

Properties of 1,8-Cineole: A Thermophysical and Theoretical Study

Santiago Aparicio, Rafael Alcalde, María J. Dávila, Begoña García, and José M. Leal*

Departamento de Química, Universidad de Burgos, 09001 Burgos, Spain

Received: November 9, 2006

This paper reports on an experimental and theoretical study of 1,8-cineole, one of the main components of essential oils in different plants. The pressure–volume–temperature behavior of this fluid was evaluated accurately over wide temperature and pressure ranges and correlated successfully with the empirical TRIDEN equation. From the measured data, the relevant derived coefficients isothermal compressibility, isobaric expansibility, and internal pressure were calculated. The isobaric heat capacities at high pressure were extrapolated from the data measured at atmospheric pressure. The cubic equations of state by Soave, Peng–Robinson, Stryjek–Vera modification of Peng–Robinson, Patel–Teja, Sako–Wu–Prausnitz, and the SAFT and PC-SAFT molecularly based equations of state were used to predict the PVT behavior. The SAFT and PC-SAFT parameters for 1,8-cineole were obtained from correlation of available saturation literature data; the best results were provided by Sako–Wu–Prausnitz and PC-SAFT equations of state, whereas the classical ones were shown to be inadequate. The molecular structure was studied by quantum computations at the B3LYP/6-311++g(d) level and classical molecular dynamics simulations in the NPT ensemble with the OPLS-AA forcefield. On the basis of both macroscopic and microscopic studies, a complex fluid structure was inferred.

Introduction

Eucalyptol (1,3,3-trimethyl-2-oxabicyclo[2.2.2]octane), also known as 1,8-cineole (CIN), is a natural constituent of the essential oil fraction of several natural sources.¹ Although worldwide available, CIN remains unexploited. A main source is the eucalyptus leaf oil, where CIN is present up to 90%. The oil released by leaves is made up of a number of volatile organic compounds, overall monoterpenes and sesquiterpenes;² among these, CIN appears to be most valuable because of its antiinflammatory and pain-releasing efficiency⁴ and antimicrobial⁵ and nematocidal properties,⁶ as well as large potential market. Recent clinical studies have shown that CIN holds back the leukaemia growth in cells;³ the readily biodegradable nature,⁷ its unreactive and nontoxic behavior,^{1a} and the wide variety of biological applications show that CIN is a benign agricultural bioagent with potentially large scale applications.

Although development of pharmaceuticals gets through some 90% of world production, CIN has found place as an efficient, chemically stable solvent for different types of compounds with industrial application. The large liquid temperature range (mp = 274.63 K; bp = 449.5 K),⁸ the moderate vapor pressure that minimizes atmospheric emissions (1160 Pa at 294 K),⁹ and its low toxicity turns CIN into a friendly compound in a green chemistry context. CIN is a valuable alternative to ozone-depleting solvents¹⁰ and is used as a fuel component; motor fuels based on gasoline mixed with vegetable oils rich in CIN¹¹ as well as use as an additive for hydrated ethanol fuel blends have been reported.¹²

The modeling of industrial processes requires knowledge of the behavior of the substances involved, otherwise inaccurate data or wrong designs may lead to either oversized costs or failure in production targets. The main drawback for a large scale application of CIN is the scarce number of reliable

chemical and physical data required in most stages of the modeling.¹³ A detailed literature search shows that most thermophysical properties of CIN refer to 25 °C, the pressure effect is left out, and either the accuracy reached is low or unclear evaluation procedures have been used. In this work the experimental pressure–volume–temperature (PVT) behavior of CIN is reported in the 278.15–358.15 K and 0.1–60 MPa ranges. From these readings the isobaric thermal expansibility, isothermal compressibility, and internal pressure were calculated; isobaric heat capacity, dynamic viscosity, speed of sound, and refractive index at atmospheric pressure have also been measured in the 298.15–343.15 K range. To attain thorough information, from the isobaric heat capacity at ambient pressure and the PVT data, the isobaric and isochoric heat capacities have been evaluated over a wider pressure range pursuing a 2-fold objective. On one hand, the above properties are required both for thermodynamic calculations and operations such as phase separation, mass transfer, power requirements, or pumping; on the other hand, these data may also provide substantial information on the fluid structure and molecular level interactions.

The modeling of thermophysical properties of fluids is a key step from practical and theoretical viewpoints. The PVT behavior of fluid mixtures is commonly described by use of the so-called equations of state (EOS), which are efficient tools for the representation of the PVT properties over wide ranges of pressure and temperature.¹⁴ Since the pioneering work by van der Waals, hundreds of EOS have been put forward with variable degree of success.¹⁴ In this work two different families of EOS have been selected. Due to the ease of handling and the accurate results provided, cubic EOS (derived from van der Waals' approach) have played a significant role both in modeling and in the development of fluid theories.¹⁵ The cubic EOS put forward by Soave (SRK),¹⁶ Peng–Robinson (PR),¹⁷ Stryjek–Vera modification of Peng–Robinson (PRSV),¹⁸ Patel–Teja (PT),¹⁹ and Sako–Wu–Prausnitz (SWP)²⁰ were used

* Corresponding author. E-mail: jmleal@ubu.es.

to predict the CIN PVT data and compared with the experimental values. Despite their growing popularity, cubic EOS suffer from several drawbacks, in particular an inaccurate representation of fluid properties.¹⁵ Therefore, classical cubic EOS have given way to molecularly based EOS, with broader theoretical background and capable of separating the interactions and quantifying the effects of structure on bulk properties and phase behavior. Among the different approaches available for the development of molecularly based EOS, due to the lower computational costs and wide pressure and temperature ranges covered, those based on Wertheim's perturbation theory have received growing recognition,²¹ giving rise to a set of EOS known as statistical associating fluid theory (SAFT).²² The original SAFT approach developed by Huang and Radosz²² and the perturbed chain (PC-SAFT)²³ version were applied to predict the CIN PVT behavior.

Molecular modeling is a powerful tool that provides a deep insight into the structure of condensed phases; combined with macroscopic studies, it may provide a good link among physicochemical properties, molecular level structure, and intermolecular interactions, thus extending the range of applications. To complete the information drawn from macroscopic measurements, a molecular modeling study of CIN combined with quantum computations at the density functional theory (DFT) level and condensed phase classical molecular dynamics simulations has been undertaken.

Experimental Section

Materials. 1,8-Cineole (Aldrich, 99% GC purity) was stored out of light over Fluka Union Carbide 0.4 nm molecular sieves to avoid moisture absorption; prior to measurements, it was degassed with ultrasound and used without further purification.

Atmospheric Pressure Measurements. All measurements at atmospheric pressure were taken in the 298.15–343.15 K temperature range. Isobaric molar heat capacity (C_p , $\pm 1 \times 10^{-2}$ J mol⁻¹ K⁻¹) was measured using a Setaram microDSC III calorimeter previously described.²⁴ Measurements were taken according to the continuous scanning method.²⁵ The heat capacity data of toluene (Fluka, >99.8%), used as reference material, and butan-1-ol (Aldrich, >99.5%), used as a calibration liquid, were obtained from the recommended values from Zabransky et al.²⁶ The temperature was controlled by peltiers to $\pm 1 \times 10^{-2}$ K.

Speed of sound, u , was determined with an Anton Paar DSA 5000 apparatus (± 0.5 m s⁻¹), the cell temperature being controlled by a built-in solid-state thermostat ($\pm 1 \times 10^{-2}$ K). The apparatus was calibrated using water (Milli-Q, resistivity 18.2 mΩ·cm) and *n*-nonane (Fluka, >99.5%) as standards. Refractive index, n_D , was measured ($\pm 5 \times 10^{-5}$) with an automated Leica AR600 refractometer whose temperature was controlled by a Julabo F32 external circulator ($\pm 1 \times 10^{-2}$ K). Calibration was performed using water and a standard supplied by the manufacturer ($n_D = 1.51416$).

Dynamic viscosity, η , was measured ($\pm 5 \times 10^{-3}$ mPa s) using an Anton Paar AMV200 rolling ball microviscometer; the temperature was controlled by a Julabo F25 external thermostat ($\pm 1 \times 10^{-2}$ K). Calibration was performed using *n*-dodecane (Aldrich, >99.5%), hexan-1-ol (Fluka, >99.5%), and decan-1-ol (Fluka, >99.5%) as standards.

High-Pressure Measurements. The apparatus used in the PVT measurements was previously described.²⁷ The system is installed around a high-pressure vibrating tube densimeter. The central element of the system is the Anton Paar DMA 512P high-pressure cell, which contains the stainless steel vibrating

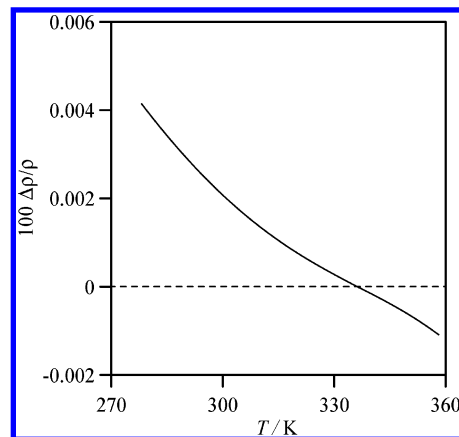


Figure 1. Percentage deviation between corrected and uncorrected density data at 0.1 MPa according to eq 1 with dynamic viscosity data from Table 1.

U-shaped tube and the electronics to excite the tube and measure the oscillating period. The cell temperature was controlled by a Julabo F32 circulating bath; a calibrating Pt100 platinum sensor located in the measuring cell connected to a $\Delta\Delta F250$ unit measures the temperature to $\pm 1 \times 10^{-2}$ K. The circuit pressure was controlled and measured by a Ruska 7615 digital pressure controller. The pressure was kept constant to $\pm 5 \times 10^{-3}$ MPa by the controller and measured to $\pm 1 \times 10^{-2}$ MPa with a pressure sensor. The pressurizing fluid was separated from the sample by a high-pressure liquid-to-liquid separator (Pressurements T3600E) which contained a Teflon diaphragm to send out the pressure. The controller and the thermometer were previously calibrated through well defined and traceable procedures. The whole system is computer controlled by a specially developed software that makes fully automatic obtaining of large amounts of accurate data feasible. The calibration procedure to turn the densimeter oscillation period into density measurements has been described.²⁷ A 14-parameter equation²⁷ was used whose values were obtained with *n*-hexane (Fluka, >99.9%) and water (Millipore, resistivity 18.2 mΩ cm) as references.⁸

The effect of sample viscosity on density measurements has been studied by several authors, who pointed out that uncertainty in measurements might increase if viscosity corrections are disregarded.²⁸ These corrections rely on both the existence of experimental viscosity data in the pressure and temperature ranges considered and properly defined and evaluated damping equations. The mathematical form of the viscosity corrections for pressures different from the atmospheric is still under study and different corrections, which basically depend on the instrument features and sample viscosity, have been suggested.²⁸ The correction factor can be evaluated with^{28a,b}

$$\frac{\Delta\rho}{\rho} = (-0.5 + 0.45\sqrt{\eta})10^{-4} \quad (1)$$

where ρ stands for the raw density data obtained according to the above procedure, $\Delta\rho$ is the difference between the raw and corrected density data, and η is the sample dynamic viscosity (mPa s). The viscosity data of CIN are reported in Table S1 (Supporting Information). Figure 1 plots the viscosity effect on the calculated densities, showing low deviations between corrected and uncorrected values; although viscosity data at higher pressures were unavailable, in view of the accuracy of all factors involved in the density determination, an accuracy of $\pm 1 \times 10^{-4}$ g cm⁻³ can be inferred for experimental raw density data without viscosity corrections.

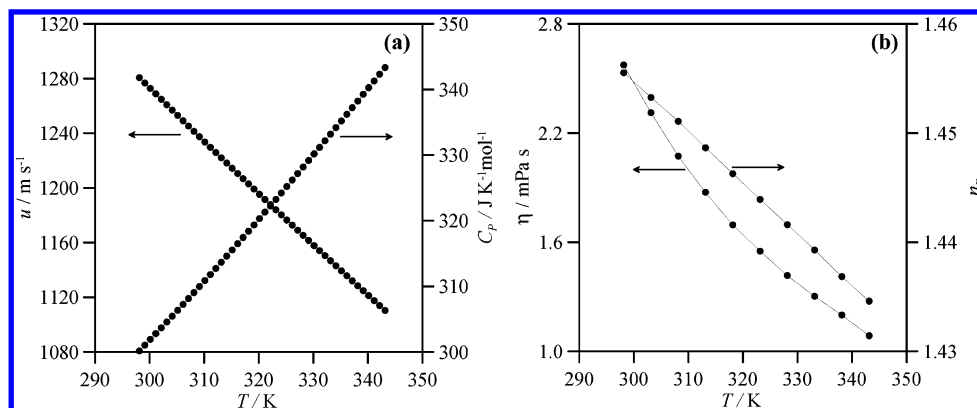


Figure 2. Experimental thermophysical properties of CIN at atmospheric pressure as a function of temperature (speed of sound, u ; refractive index, n_D ; dynamic viscosity, η ; isobaric heat capacity, C_p). Symbols: experimental data, Table S1 (Supporting Information). Lines: guide lines except for viscosity data which show an exponential fit according to the activation model.

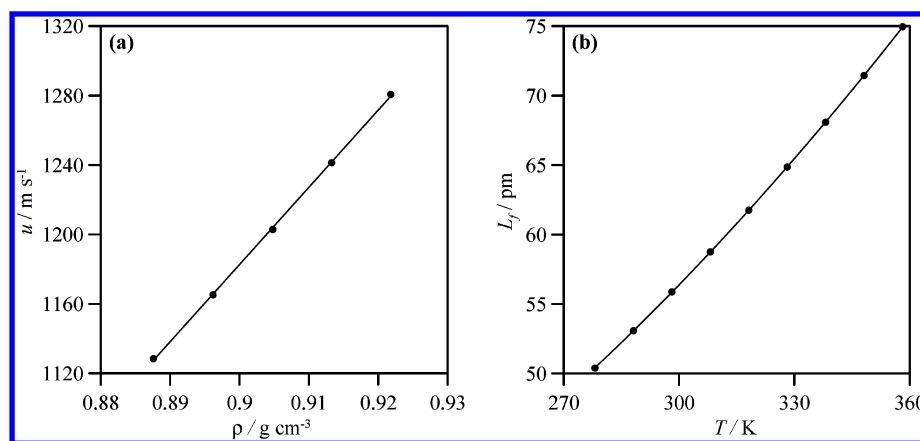


Figure 3. (a) Relation between speed of sound, u , and density, ρ , for CIN at 0.1 MPa and in the 298.15–338.15 K temperature range. (b) Temperature dependence of intermolecular free length, L_f , for CIN at 0.1 MPa. Symbols: experimental data, Tables S1 and S2 (Supporting Information). Lines: guide lines.

Quantum Calculations. Quantum calculations were carried out with the Gaussian 03 package²⁹ according to density functional theory (DFT), using the Becke gradient corrected exchange functional³⁰ and Lee–Yang–Parr correlation functional³¹ with three parameters (B3LYP)³² method. B3LYP is a gradient corrected method that includes some of the electron correlation effects. The calculations were performed at the B3LYP/6-311++g(d) level.

Molecular Dynamics Simulations. Classical molecular dynamics simulations were carried out using the TINKER molecular modeling package.³³ All simulations were performed in the NPT ensemble at 298.15 K and 0.1 MPa; the Nosé–Hoover method³⁴ was used to control the temperature and pressure of the simulation system. The motion equations were solved using the Verlet Leapfrog integration algorithm.³⁵ The molecular geometries were restrained according to shake algorithm.³⁶ Long-range electrostatic interactions were treated with the smooth particle mesh Ewald method.³⁷

The simulated system consists of a cubic box with 250 molecules to which periodic boundary conditions were applied in three directions. The simulations were performed using a cutoff $L/2$ Å radius for the nonbonded interactions, L being the box side. An initial box generated using the PACKMOL program³⁸ was minimized according to the MINIMIZE program in TINKER package to a $0.1 \text{ kcal mol}^{-1} \text{ Å}^{-1}$ rms gradient, and then a 100 ps NVT equilibration molecular dynamics simulation was run starting from the output configuration of the MINIMIZE program. Finally, from the output

NVT simulation configuration, a production run of 500 ps (time step 1 fs) in the NPT ensemble at 298.15 K and 0.1 MPa was run, from which the data were collected. CIN was described according to the so-called optimized potential for liquid simulations (*all atom* version) OPLS-AA.³⁹ This model has been applied successfully to compute liquid-state properties for different systems.⁴⁰

Results and Discussion

Atmospheric Pressure Measurements. Experimental data at atmospheric pressure are reported in Table S1 and Figure 2; speeds of sound decreased with temperature according to an almost linear trend. The relation between this property and density (Figure 3a) shows also a first-order, linear trend, as reported for different organic fluids.⁴¹ A fair analysis of the relation between speed of sound and molecular level structure can be attained introducing the concept of intermolecular free length, L_f , defined as the gap between two neighbor molecules.^{41,42} The relation between L_f and free volume is such that the larger the free volume, the longer the free length. The relation between speed of sound and free length can then be established on the basis of Eyring's free volume theory,⁴¹ according to which the acoustic wave excited in the fluid by ultrasonic measurements is momentarily sent out to the intermolecular free length, where the acoustic wave is transferred according to the speed of the fluid in the gas phase. Therefore, if L_f is long, that is, if the free volume is high, then the speed of sound is low. If one takes for granted spherical molecules,

then L_f may be estimated as⁴¹

$$L_f = 2(V_T - V_0)/Y \quad (2)$$

where V_T is the molar volume at the T temperature and V_0 is that at 0 K. The molar surface area of the molecules, Y , is calculated as

$$Y = (36\pi N_A V_0^2)^{1/3} \quad (3)$$

where V_0 is obtained according to the Sugden relation:⁴³

$$V_0 = V_T(1 - (T/T_c))^{1/3} \quad (4)$$

Here the critical temperature, T_c , is estimated according to Joback's method (661 K, Table 1).⁴⁴ The L_f values at 0.1 MPa as a function of temperature were calculated from the density values of Table S2 (Figure 3b). The optimized structure of CIN calculated at the B3LYP/6-311++g(d) level is shown in Figure 4. Although the complex shape of this molecule (C_s point group) gives rise to an intricate packaging, in a simplified view it can be regarded as being spherical, with the result of the low L_f values reported in Figure 3b and high speeds of sound. Although the free length increased with temperature, the CIN free volume is low.

Isobaric heat capacities, C_p , are reported in Table S1. Figure 2a shows the high C_p values compared to other fluids of similar size and molar mass; this property, the wide liquid temperature range (174 K), and the low vapor pressure turn CIN into a suitable option as a thermal storage energy medium.⁴⁵ The thermal storage energy, E , may be calculated as^{45b}

$$E = \rho C_p(T_{\text{out}} - T_{\text{in}}) \quad (5)$$

where T_{in} and T_{out} are the input and output temperatures of the storage medium. On the basis of the properties reported (Tables S1 and S2) and the values $T_{\text{in}} = 298.15$ K (well above the melting point) and $T_{\text{out}} = 446.15$ K (close to the boiling point), it turns out $E = 265 \text{ MJ m}^{-3}$, a value much higher (around 59 MJ m^{-3}) than those reported for common oils used in industry,^{45c} many of them explosive or inflammable.^{45b} That is, CIN can be used as an environmentally friendly alternative for thermal energy storage or heat transfer applications.

The viscosity data reported for CIN are in the range of those for common organic solvents. Even though H-bonding is lacking, the data reveal a highly structured fluid whose shape and dipolar interactions restrict the liquid flow. The viscosity/temperature data were fitted to an Arrhenius-type exponential function (Figure 2b) whose slope yielded the activation energy for viscous flow 16.2 kJ mol^{-1} ; this value amounts to 1/3 the vaporization enthalpy (48.2 kJ mol^{-1}) of most non-H-bonded organic liquids.^{9a}

The Hildebrand solubility parameter, δ ,⁴⁶ is a very useful property characteristic of solvents. Solubility parameters for CIN are not easily available due to two reasons: (i) The differences between the vaporization enthalpies (from which the parameter derives) of terpenoids are remarkable.^{9,47} (ii) Use of group contribution methods to determine δ values when experimental data are lacking is highly unreliable for compounds with fused rings, like CIN.⁴⁷ Therefore, to properly determine the δ parameter for CIN we had to fall back on the activation energy for viscous flow, E_a , according to

$$\delta = \left(\frac{3E_a - RT}{V_m} \right)^{0.5} \quad (6)$$

TABLE 1: CIN Parameters Required for the Application of Studied EOS^a

model	T_c/K	P_c/MPa	W
	661	2.84	0.3119
SWP	d 0.2167	A_0 1.7486	
SAFT	u_0/K 280.72	M 4.371	$v^{00}/\text{cm}^3 \text{mol}^{-1}$ 20.431
PC-SAFT	ϵ/K 313.66	m 3.026	$\sigma/\text{cm}^3 \text{mol}^{-1}$ 4.247

^a Critical properties calculated according to Joback's method;⁴⁴ acentric factor calculated according to the Ambrose method.⁵⁵ Other parameters obtained from simultaneous correlation of saturation pressure and saturated liquid densities between 271.15 and 371.15 K.



Figure 4. Three different views of the optimized molecular structure of CIN calculated at the B3LYP/6-311++g(d) level. The blue arrow shows the calculated dipole moment.

where V_m is the molar volume. The value $\delta = 16.5 \text{ MPa}^{0.5}$ obtained at 298.15 K, halfway through the solubility scale, reveals the CIN solvent ability for a variety of compounds. For instance, 1,1,1-trichloroethane, with $\delta = 15.8 \text{ MPa}^{0.5}$ close to that of CIN,⁴⁸ displays a well-known ozone depletion ability and is used as a cleaning and degreasing solvent; therefore, CIN could replace 1,1,1-trichloroethane advantageously in many settings with lower environmental impact. Moreover, the low viscosity values, close to those of common solvents, are adequate for efficient heat or fluid transfer operations.

The temperature effect on the refractive index (Figure 3b) is almost linear, just like for most non-H-bonded fluids. Combination of Lorentz–Lorentz's equation⁴⁹ with the refractive indices (Tables S1 and S2) leads to a classical dynamic electronic polarizability value 18.02 Å^3 for CIN; although this quantity is only slightly affected by intermolecular associations, the high value deduced points to the existence of noticeable dipolar interactions.

PVT Behavior. Experimental and calculated thermophysical properties of CIN in the 278.15–358.15 K and 0.1–60 MPa ranges are listed in Table S2 in 10 K and 5 MPa steps and plotted in Figures 5–7. The experimental compressed liquid densities were correlated with temperature and pressure according to the TRIDEN 10-parameter equation by Ihmehls and Gmehling,⁵⁰ which combines the modified Rackett equation for saturation densities with Tait's equation for isothermal compressed densities, eqs 7–9:

$$\rho_0 = \frac{A_R}{B_R [1 + (1 - T/CR)DR]} \quad (7)$$

$$\rho = \frac{\rho_0}{1 - C_T \ln \frac{B_T + P}{B_T + P_0}} \quad (8)$$

$$B_T = b_0 + b_1 \frac{T}{E_T} + b_2 \left(\frac{T}{E_T} \right)^2 + b_3 \left(\frac{T}{E_T} \right)^3 \quad (9)$$

The reference pressure $P_0 = 0.1$ MPa was used at all temperatures, and the corresponding reference densities, ρ_0 , were correlated with eq 7, the C_T Tait parameter being temperature-independent. The correlation parameters were deduced using a Levenberg–Marquardt least-squares algorithm, and the optimal fitting was assessed by the absolute average percentage deviation (AAD):

$$\text{AAD} = \frac{100}{N} \sum_{j=1}^N \left| \frac{\rho_{i,\text{EXP}} - \rho_{i,\text{CAL}}}{\rho_{i,\text{EXP}}} \right| \quad (10)$$

Here N is the number of data pairs. Table S3 summarizes the fitting parameters deduced.

The density values (Figure 5a) dropped when the temperature was raised along isobars and increased when the pressure was raised along isotherms. Although the CIN free volume is relatively low, the bulky nature and complex shape along with the preferential dipolar orientations give rise to densities slightly lower than those for fluids with similar features and molar mass. The ether bridging site of CIN is sterically hampered by the presence of the neighbor methyl groups; hence, the configuration order around this group is disrupted, the packaging becomes slightly inefficient, and the dipolar forces become weakened. Likewise the low O to C atoms ratio also bear a part of the density effect. In short, the densities are in the range of common organic solvents and CIN can replace with same efficiency and reliability those with less favorable profile.

The derived properties isobaric thermal expansivity, α_P , isothermal compressibility, κ_T , and internal pressure, P_i , were all evaluated by application of well-known relations²⁷ to the PVT measurements and the TRIDEN fitting coefficients (Table S3); the excellent fitting obtained has enabled a fair description of the PVT behavior, the function put forward is consistent, and the derived properties calculated were fairly accurate. Figure 5b plots the behavior of isobaric thermal expansivity; the α_P values decreased when pressure was increased along isotherms because of the diminution of free volume, whereas the observed trend along isobars shows quite an interesting anomaly. Most fluids, even water, showing some sort of thermodynamic anomalies, present increasing α_P values as the temperature is raised along isobars; in fact, the data for CIN at low pressures concur with the regular behavior, but at high pressures ($P > 25$ MPa) the α_P values pass through a maximum. This feature indicates a sign change in the slope $(\partial\alpha_P/\partial T)_P$ not only from one isobar to another but also along the same isobar (at high pressure) from positive (low temperature) to negative (high temperature) values. This unusual downward trend of α_P with increasing temperature has been reported earlier for alkanols at low temperatures,^{51a} lubricants,^{51b} and ionic liquids^{51c,d} and reinforced by molecular simulation.^{51f} Some authors put down such a striking feature to the high degree of liquid ordering;^{52a} others, however, bear in mind anharmonic intermolecular vibrations and their effect on the variation of the intermolecular potential with pressure and temperature.^{52b}

Evaluation of α_P values of most fluids from density/temperature data pairs suffers from difficulties inherent to the mild deviation from linearity; in this work the fitting of the TRIDEN equation to the PVT surface yielded accurate α_P values, independent of the particular fitting function. The values for CIN, in the range of those for common organic fluids, showed the subtle effect of a noticeable 12% falloff in α_P with

rising temperature at 60 MPa, well beyond the error limit. In contrast, the isothermal compressibilities κ_T markedly tended to decrease with pressure along isotherms and to increase with temperature along isobars (Figure 6a), concurrent with the diminution of free intermolecular space. The fluid becomes less compressible as the pressure rises, and at high enough pressures it approaches a compressibility value corresponding to the closest packed volume. Although the highest pressure was insufficient to reach such a point, the temperature effect on κ_T decreased as the pressure was raised; for instance at 0.1 MPa a temperature increase from 278.15 to 358.15 K brought about 66.91% increase in κ_T , but at 60 MPa it only reached 37.85%. Compared to other common organic fluids, the pronounced pressure effect on κ_T can be put down to the spherical CIN shape. At higher pressures a larger decrease of free volume was observed due to the more efficient packaging associated with the remarkable decrease of κ_T .

Internal pressure, defined as $P_i = (\partial U/\partial V)_T$, represents the work exerted against the cohesive forces by a liquid that undergoes an isothermal expansion entailing a change in internal energy (Figure 6b).⁵³ P_i may be regarded as a measure of nonchemical interactions in a fluid;⁵³ however, large dipolar interactions are not perceived by P_i because they restrict the molecular movement in a way similar to that by hydrogen bonding, which is included in the so-called cohesive energy density but not in P_i .⁵³ The pressure and temperature effects on P_i measure the strength of the most important intermolecular forces. The P_i values deduced for CIN point to relatively strong attraction forces, 54.8 kJ mol⁻¹ at 298.15 K and 0.1 MPa; despite the low dipole moment (1.57 D, calculated at B3LYP/6-311++g(d) theoretical level), this large nonchemical interaction energy can be put down to the high polarizability of CIN.⁵³ The P/T behavior of P_i is complex (Figure 6b). At low temperatures P_i increases with increasing pressure, but the trend is inverted at high temperatures; along isobars a maximum appears. These features justify the α_P anomaly and are related to an important fluid ordering regardless the low dipole moment value.

Isobaric heat capacities, C_P (Figure 7a, Table S2), were calculated from the PVT data as

$$\left(\frac{\partial C_P}{\partial P} \right)_T = -T \left(\alpha_P^2 + \left(\frac{\partial \alpha_P}{\partial T} \right)_P \right) \quad (11)$$

where eq 11 was numerically integrated using the C_P measurements at 0.1 MPa reported in Table S1. As expected, the C_P values rised remarkably with increasing temperature; the pressure effect on C_P was mild at 278.15 K, only ~ 0.08 J mol⁻¹ K⁻¹ MPa⁻¹, and for most of the isotherms C_P decreased slightly with increasing pressure. However, a boost to temperature brings about the diminution of the C_P/P slope, and then at high temperatures it goes through a minimum followed by further increase with increasing pressure. This unusual feature is related to the α_P behavior, since both properties bear relation in the form

$$\left(\frac{\partial C_P}{\partial P} \right)_T = -T \left(\frac{\partial^2 V}{\partial T^2} \right)_P \quad (12)$$

The growing trend of C_P with increase in pressure only appears at the highest temperatures. This mild effect reveals a remarkable structural ordering in CIN; for instance at 358.15 K an increase in pressure from 20 to 60 MPa gives rise to only 1.70% increase in C_P (0.16 J mol⁻¹ K⁻¹ MPa⁻¹), and thus it is very sensitive to experimental and calculation errors. According

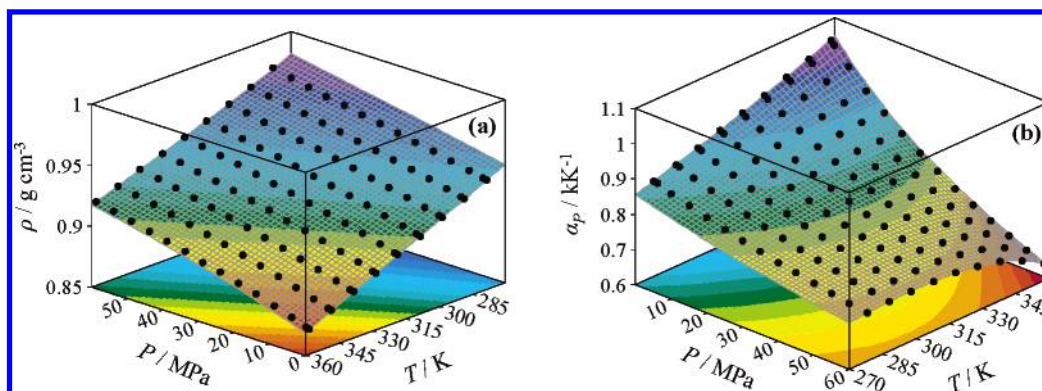


Figure 5. Experimental density, ρ , and calculated isobaric thermal expansivity, α_p , for CIN as a function of pressure and temperature. Contour plots are plotted at the bottom of the figures.

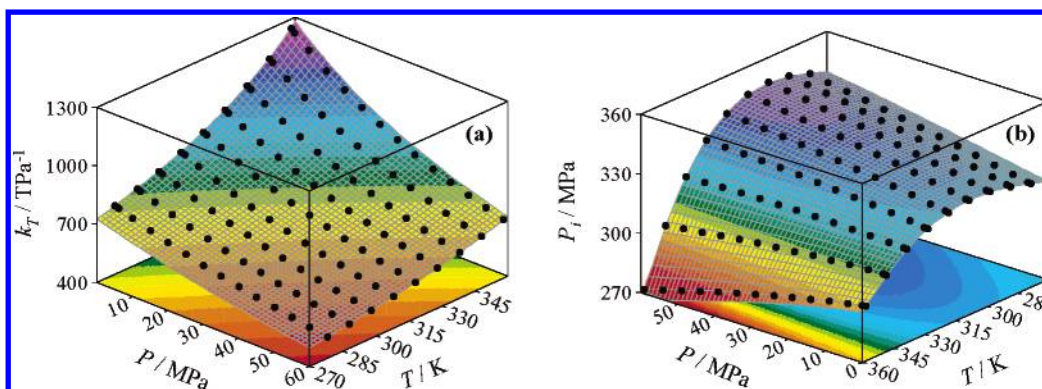


Figure 6. Calculated isothermal compressibility, k_T , and internal pressure, P_i , for CIN as a function of pressure and temperature. Contour plots are plotted at the bottom of the figures.

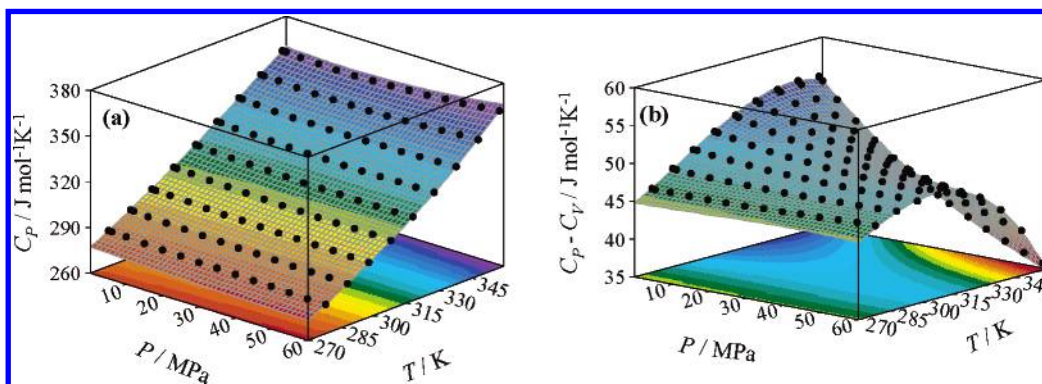


Figure 7. Experimental (0.1 MPa data) and calculated (other pressures) isobaric heat capacity, C_p , and difference between isobaric and isochoric heat capacity, $C_p - C_v$, for CIN as a function of pressure and temperature. Contour plots are plotted at the bottom of the figures.

to eq 11 the main source of uncertainty arises from the experimental calorimetric data at 0.1 MPa used in the integration. The high accuracy of these data is conveyed to the C_p values calculated at other pressures; hence, the C_p anomaly stands for reason because it is well below the uncertainty of the calculated C_p and still becomes more remarkable as the temperature is raised. The isochoric heat capacity values, C_v , reported in Table S2 show the same behavior as C_p ; even so, the anomaly appears at lower temperatures. The observed $C_p - C_v$ difference (Figure 7b), set down to the intermolecular forces in the fluid, shows a complex behavior in the P/T range studied. The values reported were high enough; that is, despite the low dipole moment, the CIN molecules interact remarkably, concurrent with the above conclusions.

Equations of State. The predictive ability of cubic and molecularly based EOS was tested in this work. Application of the models require critical properties for CIN, but these are not experimentally available; therefore they were calculated (e.g.,

acentric factor) from group contribution methods (Table 1).^{44,55} The equations and required parameters may be found in the original EOS papers^{16–23} and in previous works.^{24,27} SWP, SAFT, and PC-SAFT parameters, unavailable for CIN, were obtained from parallel correlation of saturation pressure and saturated liquid density according to a least-squares procedure (Table 1). Literature saturation properties for CIN are scarce and confusing; the saturation pressures reported^{9b,c} are contradictory and did not match up well with those at lower temperatures.^{9a} Therefore, only the data by Stull were considered for the correlation.⁵⁴ Likewise, saturated liquid density literature data were unavailable and were calculated under P/T saturation conditions⁵⁴ using the TRIDEN parameters reported in Table S3. Results from correlations, saturation properties and predictions, and compressed liquid densities are reported in Table 2.

Application of predictive cubic EOS to saturation pressure and saturated densities gave rise to highest deviations. SRK, with the highest density deviations under saturation and

TABLE 2: Absolute Average Percentage Deviation, AAD, for the Correlation of Saturation Properties and Prediction of Compressed Liquid Density^a

model	AAD satn pressure	AAD satd liquid density	$\Delta T_C/K$	$\Delta P_C/MPa$	AAD compressed liquid density
SRK	5.64	12.36			10.64
PR	17.60	0.76			2.66
PRSV	2.09	0.70			2.71
PT	15.20	0.79			2.86
SWP	1.30	0.05	-4.00	0.14	1.14
SAFT	0.88	0.99	43.74	0.47	2.13
PC-SAFT	0.48	0.08	23.80	0.54	1.08

^a Model parameters from Table 1. $\Delta T_C = T_{C,EOS} - T_C$ and $\Delta P_C = P_{C,EOS} - P_C$.

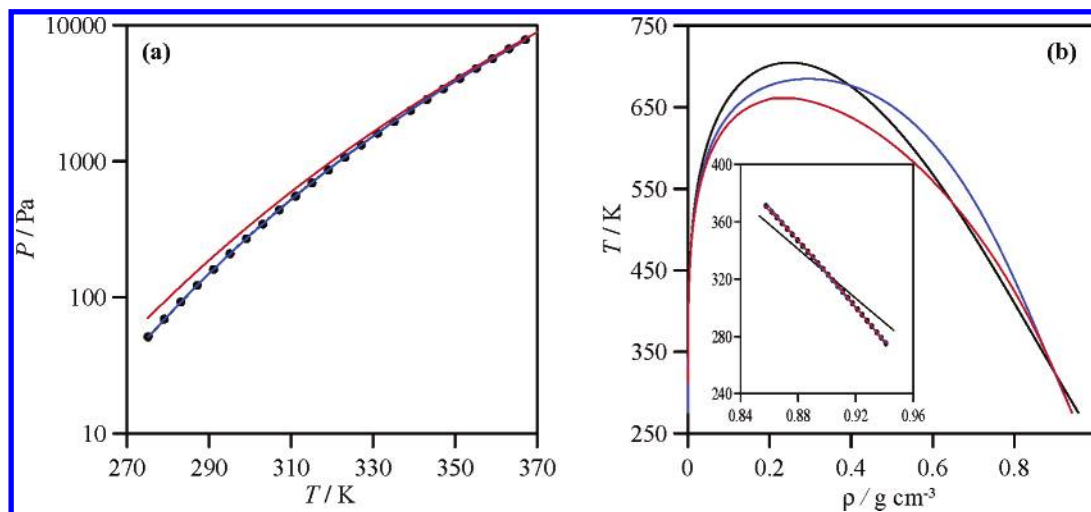


Figure 8. (a) Saturation pressure and (b) saturated liquid and vapor density for CIN: (●) experimental saturated pressure from ref 54 and saturated liquid densities calculated using eqs 7–9 and parameters in Table S3 (Supporting Information) under the experimental saturation conditions from ref 54; (black line) SAFT; (blue line) PC-SAFT; (red line) SWP. Model parameters are from Table 1.

compressed liquid conditions, was the worse predictive model. PR and PRSV gave rise to similar results; PRSV improved the saturation pressure predictions but not the densities, even though density deviations were too high for the models. The PT 3-parameter EOS yielded predictions close to that from PR, without any remarkable improvement compared to simpler models. In summary, the most frequent cubic EOS are prone to flaws and deviations ascribable to the complex structure of pure CIN. Despite its higher predictive ability, SWP was not commonly used for modeling of complex fluids.²⁷ This model is, in principle, well-suited for systems strongly nonideal or with structured complex molecules like CIN; it contains an additional interaction parameter that measures the external rotational and vibrational degrees of freedom. SWP gives rise to the lowest deviations, correlates successfully the saturation conditions (Figure 8), and predicts compressed liquid density with quality similar to molecular based EOS (Figure 9).

Among molecularly based EOS, PC-SAFT constitutes a remarkable improvement in relation to both cubic EOS and the original SAFT version.²³ The SAFT correlation of saturation properties was successful but led to overpredicted critical properties (Table 2); like for any mean field approach, this could be corrected by fitting the model parameters to the critical properties⁵⁶ or by a crossover equation,⁵⁷ an objective beyond the scope of this work. The lower quality compressed liquid density predictions (Figure 9) were similar to those by cubic EOS, but they were worse compared to SWP; hence, the improvement provided does not make up for the harder computational effort paid. PC-SAFT is capable of predicting successfully phase equilibria and PVT behavior for a variety of pure compounds with only small vapor pressure and volume deviations; compared to the original SAFT model, the improved correlation is confirmed for CIN, for which PC-SAFT leads to

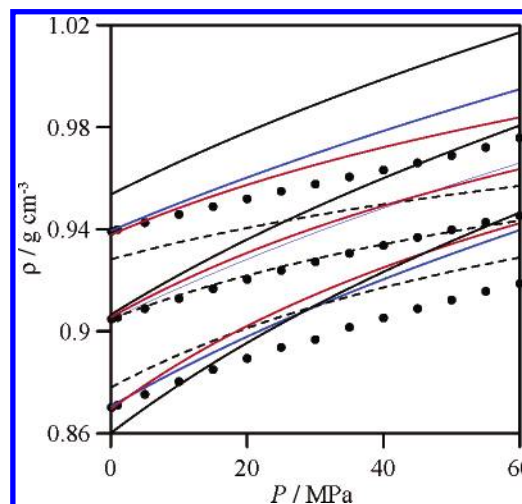


Figure 9. Experimental and calculated compressed liquid densities, ρ , at 278.15, 318.15, and 358.15 K (from top to bottom) for CIN: (●) experimental data; (black line) SAFT; (blue line) PC-SAFT; (red line) SWP; (---) PR. Model parameters are from Table 1.

lower deviations. Saturation conditions are pretty well correlated (Figure 8), and although critical properties appear over predicted, the deviations fall off. The compressed liquid deviations increase as pressure rises, but in light of the wide pressure and temperature ranges studied, the PVT predictions reached can be regarded as satisfactory. If a purely mathematical parameter fitting had been done, then of course better correlations and predictions could have been reached with both SAFT and PC-SAFT models. However, in view that a main strength of molecularly based EOS is the physically meaningful parameters they provide (a major argument used to support the model

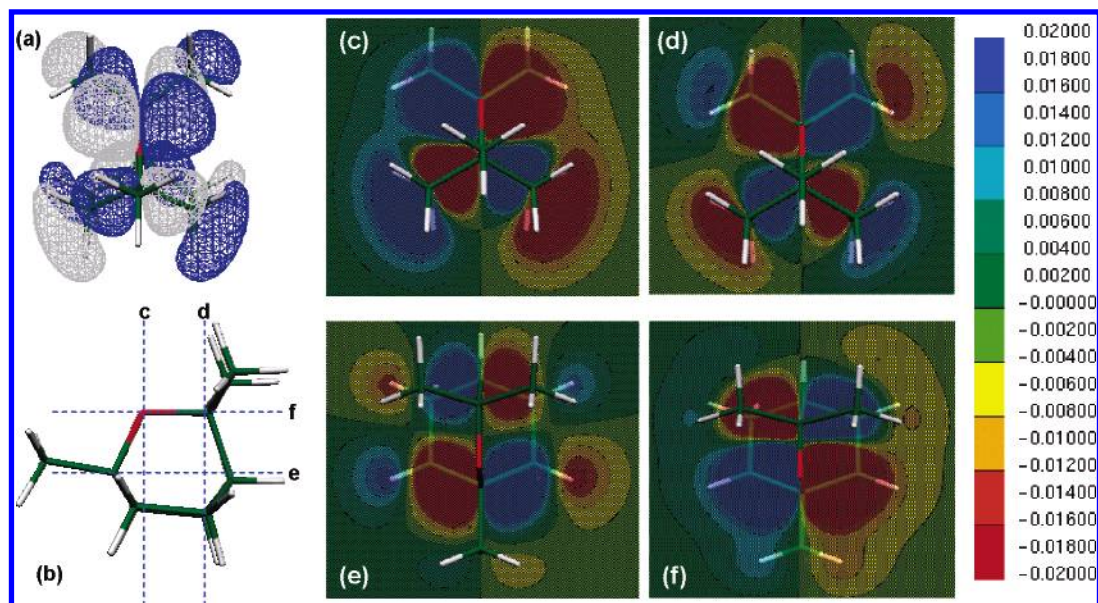


Figure 10. (a) Calculated, B3LYP/6-311++g(d), HOMO surfaces for CIN at an isosurface value of $0.02 \text{ e}/\text{\AA}^3$ and (c–f) slices through the HOMO at planes indicated in (b).

supremacy), to keep the concurrence with physics they should be maintained within certain limits.⁵⁸ Thus, SWP, among cubic EOS, and PC-SAFT, among molecularly based, most adequately describe the CIN properties in the P/T range considered.

Quantum Calculations. Figure 4 shows the lowest energy CIN structure calculated at the B3LYP/6-311++g(d) theoretical level, and Table S4 lists the molecular parameters. The optimized structure is highly complex, with the cyclohexyl ring and the oxygen ring in orthogonal positions. The dipole moment placed in the oxygen ring pointing to the opposite vortex of the cyclohexyl ring conditions the dipolar interaction. The dipolar vector embedded in the central ring gives rise to preferential orientations among the neighbor CIN molecules and to a slightly ineffective packaging reflected by the lower CIN density compared to related molecules. The molecular orbitals of CIN, also complex, exhibit different symmetries and locations. The phase pattern of the HOMO orbital (Figure 10) is highly symmetrical around the central ring formed by the ether oxygen. The CIN molecule has C_s symmetry, with the dipole moment in the mirror plane of the oxygen ring. Therefore, the frontier orbitals HOMO, HOMO-1, HOMO-2, and LUMO (Figure 11) are A' and A'' symmetry; hence, mixing is prohibited. The HOMO slices (Figure 10) show the electron density evolution along the oxygen ring. Slices c and d show the change of the phase pattern on going from the O atom toward the two methyl groups as it happens with slices e and f in which the height over the cyclohexyl ring rises. The HOMO arises from combination of the p_z -O orbitals with the p_z -C orbitals with remarkable contributions of s-C orbitals mainly from those of the methyl substituents, C_{10} and C_{11} (Figure S1, Supporting Information, and Table 3). The HOMO-1 structure, with A'' symmetry (Figure 11), differs from the HOMO; the orbital coefficients (Table 3) show that this orbital consists of p_x – p_y orbitals with some s-orbital contribution mainly from the methyl substituents. The LUMO structure shows an in-phase distribution along the cyclohexyl ring with antiphase regions below and behind.

Molecular Dynamics Simulation. The information deduced from molecular dynamics simulations enables a molecular analysis of the CIN structure. Radial distribution functions (RDF) are used to infer microstructural features of fluids, such

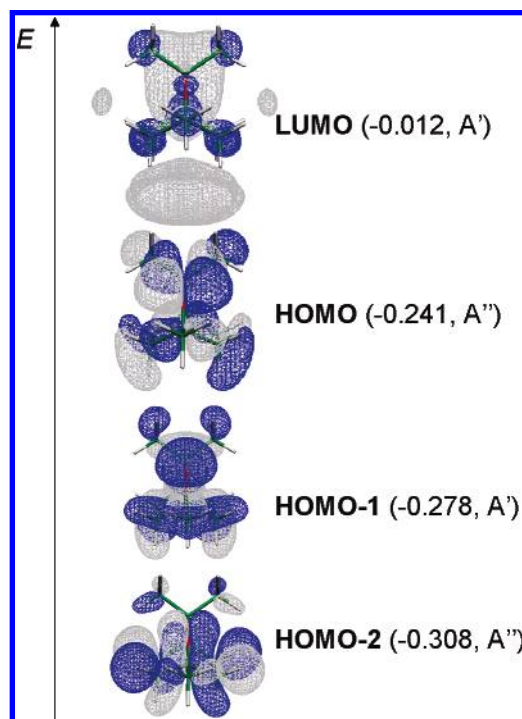


Figure 11. (a) Calculated, B3LYP/6-311++g(d), molecular orbitals for CIN at an isosurface value of $0.02 \text{ e}/\text{\AA}^3$. Parenthesized values show eigenvalues and symmetry for each orbital.

as aggregation or preferential orientation. Some RDFs (Figure 12) of CIN reveal a remarkable fluid structuring extended to long distance. The O–O RDF reported shows two sharp peaks at 6.05 and 8.05 \AA , pointing to a certain structuring around the CIN oxygen. The appearance of less intense maxima at higher distances shows the prevalence of the former. The arrangement of C atoms around the O atom also is shown in Figure 12a; RDFs for the substituent atoms in the central ring, C_9 and C_{10} atoms, are reported (Figure 1). The RDFs for both atoms show similar features, with a first sharp peak at 6.15 \AA and complex behavior at longer distances. The RDF for the C_{10} atom (similar to that for the symmetric C_{11}) is only slightly less intense than

TABLE 3: Molecular Orbital Coefficients of HOMO and HOMO-1 for CIN Calculated at the B3LYP/6-311++g(d) Level^a

					HOMO					
atom orbital	1C(5s)	2C(4s)	2C(4p _z)	2C(5s)	3C(4s)	3C(4p _z)	3C(5s)	4C(3p _z)	5C(5p _z)	6C(5s)
orbital coeff	0.18	0.11	−0.11	0.25	−0.11	−0.11	−0.25	0.12	0.10	−0.18
atom orbital	7O(2p _z)	7O(3p _z)	7O(4p _z)	8C(5p _z)	10C(4s)	10C(4p _z)	10C(5s)	11C(4s)	11C(4p _z)	10C(5s)
orbital coeff	−0.24	−0.35	−0.36	−0.60	0.14	−0.10	0.65	−0.14	−0.10	−0.65
					HOMO-1					
atom orbital	1C(5s)	4C(3p _x)	4C(5s)	5C(2p _x)	5C(3p _x)	5C(4p _x)	6C(5s)	7O(2p _x)	7O(2p _y)	7O(3p _x)
orbital coeff	0.10	0.13	0.22	−0.11	−0.16	−0.16	0.10	−0.13	−0.10	−0.19
atom orbital	7O(3p _y)	7O(4s)	7O(4p _x)	7O(4p _y)	8C(3p _x)	8C(3p _y)	8C(5s)	9C(5s)	10C(5s)	11C(5s)
orbital coeff	−0.14	−0.12	−0.18	−0.14	0.14	0.11	0.22	−0.20	−0.16	−0.16

^a Only reported atom orbitals with absolute value of their coefficients greater than 0.1. Atom numbering as in Figure S1 (Supporting Information).

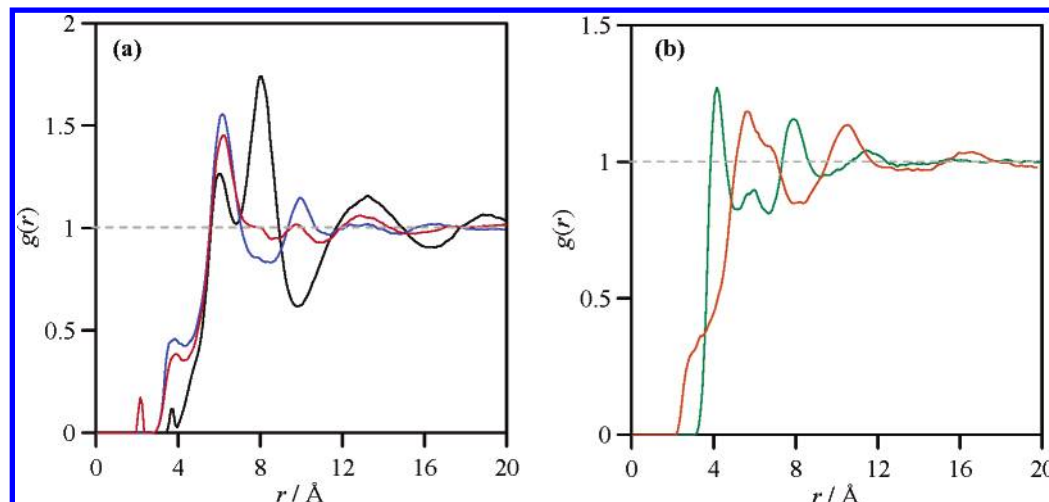


Figure 12. Site-site radial distribution functions for CIN at 298.15 K and 0.1 MPa: (black line) O7–O7; (blue line) O7–C9; (red line) O7–C10; (green line) C9–C10; (orange line) O7–H12. The numbering for each atom type is as in Figure S1 (Supporting Information).

that for C₈, and the behavior at longer distances points to a less effective structuring than for C₈, which shows a second maximum at 10 Å. This feature could be justified by the presence of two carbon atoms, C₁₀ and C₁₁, in the same ring site. An interaction with the oxygen could be established, and thus, it is slightly more hindered than the C₈ atom; this effect seems to be only remarkable at longer distances because the first peak is only slightly less intense.

Figure 12b shows the RDF for the C₈–C₁₁ atoms. The first peak at 4.15 Å and the second at 8.05 Å show a certain extent of correlation between both atoms because they interact almost equivalently with the O site. The RDFs for the O7–H₁₂ atoms enable us to rule out hydrogen bonding; although a peak appeared at 5.65 Å, the distance is too high and the peak too broad for such an interaction.

Quantitative prediction of physical properties of fluids from molecular simulations is an extremely important tool not only because of the importance of such properties but also because accurate predictions validate the available force fields and provide a fair connection between molecular level models and the macroscopic properties intimately related to the microscopic fluid structure. Although the objective of this work is far from providing an extensive molecular dynamics study of the CIN properties, the experimental properties can readily be compared to some values obtained from the simulations. A snapshot of the molecular dynamics simulation displaying (a) all the atoms (Figure 13a) and (b) only the O atoms (Figure 13b) shows a complex CIN molecular picture. The O atoms seem to determine the fluid structure with a certain extent of clustering in different places of the fluid. Density is an important property for the

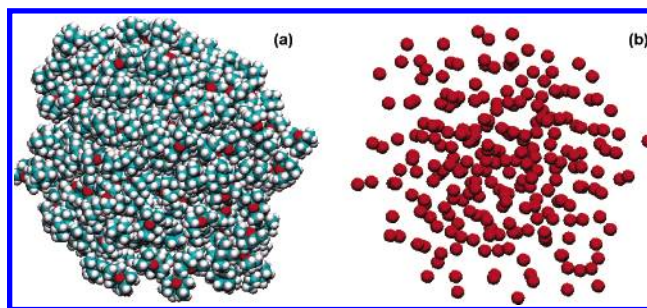


Figure 13. Molecular dynamics snapshot of CIN from 500 ps simulation: oxygen (red); carbon (blue); hydrogen (gray).

characterization of fluids that can be obtained from simulation in a straightforward manner. The value obtained from simulations for CIN at 298.15 K and 0.1 MPa, 0.9337 g cm^{−3}, only 1.3% greater than the measured value (Table S2), reveals that OPLS-AA is a reliable force field and the density predictions are better than those obtained with most available EOS.

Dynamic properties are important quantities, not easily measurable, to characterize fluids. The self-diffusion coefficient, *D*, is calculated from Einstein's relation:

$$D = \frac{1}{6} \lim_{t \rightarrow \infty} \langle \Delta r(t)^2 \rangle \quad (13)$$

Here the quantity in brackets, the mean square displacement, msd, is plotted in Figure 14 for the first 10 ps of the simulation. The slope of the linear fitting found for msd for *t* > 5 ps, Figure 4, yields *D*_{CIN} = 0.449 × 10^{−9} m² s^{−1}, a value of the same

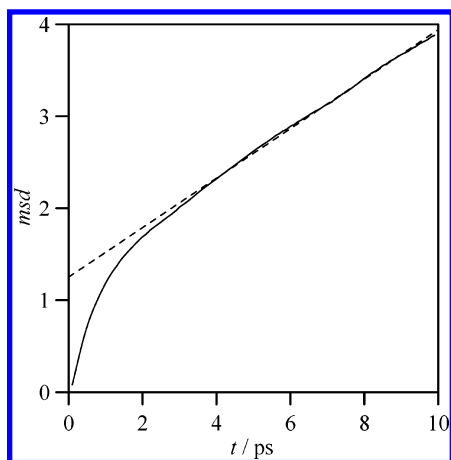


Figure 14. (—) Center of mass mean square displacement, msd, of CIN at 298.15 and 0.1 MPa and (---) linear fit of the linear part of msd.

order as those for common organic fluids. From the Einstein–Stokes relation and the viscosity values (Table S1), the hydrodynamic radius, $r = 1.89 \text{ \AA}$, was deduced for CIN.

Concluding Remarks

This work reports on a combined experimental and theoretical study on the structure and properties of CIN. The fluid behavior reveals a number of anomalies related to the structural fluid complexity, such as a falloff of α_P values with rising temperature along isobars or the increase in C_P as pressure is raised along isotherms. These properties turn CIN into a suitable candidate for a number of applications. The theoretical study shows the existence of a certain structural ordering extended to long distances around the O site without H-bonding. The molecular dynamics study according to the OPLS-AA force field provides a reliable description of the fluid structure and an efficient tool to predict fluid properties.

Acknowledgment. The financial support by Junta de Castilla y León, Project BU10/03, and Ministerio de Educación y Ciencia, Project CTQ2005-06611/PPQ (Spain), is gratefully acknowledged.

Supporting Information Available: Atmospheric pressure properties (Table S1), density, isobaric thermal expansivity, isothermal compressibility, internal pressure, and isobaric and isochoric heat capacity values (Table S2), TRIDEN fitting coefficients of density as a function of pressure and temperature (Table S3), an optimized CIN structure (Figure S1), and molecular parameters (Table S4). This material is available free of charge via the Internet at <http://pubs.acs.org>.

References and Notes

- (1) (a) De Vincenzi, M.; Silano, M.; De Vincenzi, A.; Maiale, F. C.; Scazzocchio, B. *Fitoterapia* **2002**, 73, 269. (b) Guenther, E. *The Essential Oils*; Van Nostrand: NJ, 1949.
- (2) (a) Nicolle, D.; Dunlop, P. J.; Bignell, C. M. *Flavour Fragrance J.* **1998**, 13, 324. (b) Barton, A. F. M.; Tjandra, J.; Nicholas, P. G. *J. Agric. Food Chem.* **1989**, 37, 1253.
- (3) Moteki, H.; Hibasami, H.; Yamada, Y.; Katsuzaki, H.; Imai, K.; Komiyama, T. *Oncol. Rep.* **2002**, 9, 757.
- (4) (a) Levison, K. K.; Takayama, K.; Isowa, K.; Okabe, K.; Nagai, T. *J. Pharm. Sci.* **1994**, 83, 1367. (b) Yamane, M. A.; Williams, A. C.; Barry, B. W. *Int. J. Pharm.* **1995**, 116, 237.
- (5) Gundidza, M.; Deans, S. G.; Kennedy, A. L.; Mavi, S.; Watnann, P. G.; Gray, A. L. *J. Sci. Food Agric.* **1993**, 63, 361.
- (6) Sangwan, N. K.; Verma, B. S.; Verma, K. K.; Dhindsa, K. S. *Pestic. Sci.* **1990**, 28, 331.
- (7) (a) Opdyke, D. L. *Food Cosmet. Toxicol.* **1975**, 13, 91. (b) Haley, T. J. *Dangerous Prop. Ind. Mater. Rep.* **1982**, 2, 10.
- (8) Lemmon, E. W.; McLinden, M. O.; Friend, D. G. Thermophysical Properties of Fluid Systems. In *NIST Chemistry WebBook, NIST Standard Reference Database Number 69*; Linstrom, P. J., Mallard, W. G., Eds.; National Institute of Standards and Technology: Gaithersburg, MD 20899, March 2003 (<http://webbook.nist.gov>).
- (9) (a) Armstrong, P. A.; Carless, J. E.; Enever, R. P. *J. Pharm. Pharmacol.* **1971**, 23, 473. (b) Hazra, A.; Alexander, K.; Dollimore, D.; Riga, A. J. *Therm. Anal. Calorim.* **2004**, 75, 317. (c) Hazra, A.; Dollimore, D.; Alexander, K. *Thermochim. Acta* **2002**, 221, 392.
- (10) (a) Barton, A. F. M. *Chem. Aust.* **1997**, 64, 4. (b) Soh, M.; Stachowiak, G. W. *Flavour Fragrance J.* **2002**, 17, 278.
- (11) Takeda, S.; Hoki, M. *Mie Daigaku Nogakubu Gakujutsu Hokoku* **1982**, 64, 5.
- (12) (a) Barton, A. F. M.; Tjandra, J. *Fluid Phase Equilib.* **1988**, 44, 117. (b) Barton, A. F. M.; Tjandra, J. *Fuel* **1989**, 68, 11.
- (13) (a) Lahlou, M. *Phytother. Res.* **2004**, 18, 435. (b) Reverchon, E. J. *Supercrit. Fluid* **1997**, 10, 1. (c) Azevedo, E. G.; Matos, H. A.; Nunes da Ponte, M.; Simões, P. C. *Proc. First Int. Symp. Supercrit. Fluids*; Nice, France, ISASF: 1988. (d) Matos, H. A.; Azevedo, E. G.; Simões, P. C.; Carrondo, M. T.; Nunes da Ponte, M. *Fluid Phase Equilib.* **1989**, 52, 357. (e) Francisco, J. C.; Sivik, B. J. *Supercrit. Fluid* **2002**, 23, 11.
- (14) Sengers, J. V.; Kayser, R. F.; Peters, C. J.; White, H. J., Eds. *Equations of State for Fluids and Fluid Mixtures*; Elsevier: Amsterdam, 2000.
- (15) Valderrama, J. O. *Ind. Eng. Chem. Res.* **2003**, 42, 1603.
- (16) Soave, G. *Chem. Eng. Sci.* **1972**, 27, 1197.
- (17) Peng, D.; Robinson, D. *Ind. Eng. Chem. Fundam.* **1976**, 15, 59.
- (18) Stryjek, R.; Vera, J. H. *Can. J. Chem. Eng.* **1986**, 64, 323.
- (19) Patel, N.; Teja, A. *Chem. Eng. Sci.* **1982**, 37, 463.
- (20) Sako, T.; Wu, A. H.; Prausnitz, J. M. *J. Appl. Polym.* **1989**, 38, 1839.
- (21) Wertheim, M. S. *J. Chem. Phys.* **1986**, 85, 2929.
- (22) (a) Chapman, W. G.; Gubbins, K. E.; Jackson, G.; Radosz, M. *Ind. Eng. Chem. Res.* **1990**, 29, 1709. (b) Huang, S. H.; Radosz, M. *Ind. Eng. Chem. Res.* **1990**, 29, 2284.
- (23) Gross, J.; Sadowski, G. *Ind. Eng. Chem. Res.* **2001**, 40, 1244.
- (24) Alcalde, R.; Aparicio, S.; García, B.; Dávila, M. J.; Leal, J. M. *New J. Chem.* **2005**, 29, 817.
- (25) Cerdeiría, C. A.; Míguez, J. A.; Carballo, E.; Tovar, C. A.; de la Puente, E.; Román, L. *Thermochim. Acta* **2000**, 347, 37.
- (26) Zabransky, M.; Ruzicka, V.; Mayer, V.; Domalski, E. S. Heat Capacities of Liquids. Critical Review and Recommended Values. *J. Phys. Chem. Ref. Data* **1996**, Monograph No. 6.
- (27) (a) García, B.; Aparicio, S.; Alcalde, R.; Dávila, M. J.; Leal, J. M. *Ind. Eng. Chem. Res.* **2004**, 43, 3205. (b) Aparicio, S.; García, B.; Alcalde, R.; Dávila, M. J.; Leal, J. M. *J. Phys. Chem. B* **2006**, 110, 6933.
- (28) (a) Fandiño, O.; Pensado, A. S.; Lugo, L.; López, E. R.; Fernández, J. *Green Chem.* **2005**, 7, 775. (b) Lundström, R.; Goodwin, A. R. H.; Hsu, K.; Frels, M. F.; Caudwell, D. R.; Trusler, J. P. M. *J. Chem. Eng. Data* **2005**, 50, 1377. (c) Bernhardt, J.; Pauly, H. *J. Phys. Chem.* **1980**, 84, 145. (d) Ashcroft, S. J.; Booker, D. R.; Turner, J. C. R. *J. Chem. Soc., Faraday Trans.* **1990**, 86, 145.
- (29) Frisch, M. J.; Trucks, G. W.; Schlegel, H. B.; Scuseria, G. E.; Robb, M. A.; Cheeseman, J. R.; Montgomery, J. A., Jr.; Vreven, T.; Kudin, K. N.; Burant, J. C.; Millam, J. M.; Iyengar, S. S.; Tomasi, J.; Barone, V.; Mennucci, B.; Cossi, M.; Scalmani, G.; Rega, N.; Petersson, G. A.; Nakatsuji, H.; Hada, M.; Ehara, M.; Toyota, K.; Fukuda, R.; Hasegawa, J.; Ishida, M.; Nakajima, T.; Honda, Y.; Kitao, O.; Nakai, H.; Klene, M.; Li, X.; Knox, J. E.; Hratchian, H. P.; Cross, J. B.; Adamo, C.; Jaramillo, J.; Gomperts, R.; Stratmann, R. E.; Yazyev, O.; Austin, A. J.; Cammi, R.; Pomelli, C.; Ochterski, J. W.; Ayala, P. Y.; Morokuma, K.; Voth, G. A.; Salvador, P.; Dannenberg, J. J.; Zakrzewski, V. G.; Dapprich, S.; Daniels, A. D.; Strain, M. C.; Farkas, O.; Malick, D. K.; Rabuck, A. D.; Raghavachari, K.; Foresman, J. B.; Ortiz, J. V.; Cui, Q.; Baboul, A. G.; Clifford, S.; Cioslowski, J.; Stefanov, B. B.; Liu, G.; Liashenko, A.; Piskorz, P.; Komaromi, I.; Martin, R. L.; Fox, D. J.; Keith, T.; Al-Laham, M. A.; Peng, C. Y.; Nanayakkara, A.; Challacombe, M.; Gill, P. M. W.; Johnson, B.; Chen, W.; Wong, M. W.; Gonzalez, C.; Pople, J. A. *Gaussian 03*, revision C.02; Gaussian, Inc.: Wallingford, CT, 2004.
- (30) Becke, A. D. *Phys. Rev. A* **1988**, 38, 3098.
- (31) Lee, C.; Yang, W.; Parr, R. G. *Phys. Rev. B* **1988**, 37, 785.
- (32) Becke, A. D. *J. Chem. Phys.* **1993**, 98, 5648.
- (33) Ponder, J. W. *TINKER: Software tool for molecular design*, 4.2 ed.; Washington University School of Medicine: St. Louis, MO, 2004.
- (34) Hoover, W. G. *Phys. Rev. A* **1985**, 31, 1695.
- (35) Allen, M. P.; Tildesley, D. J. *Computer Simulation of Liquids*; Clarendon Press: Oxford, U.K., 1989.
- (36) Rickaert, J. P.; Cicciotti, G.; Berendsen, H. J. J. *Comput. Phys.* **1977**, 23, 327.
- (37) Essmann, U. L.; Perera, M. L.; Berkowitz, T.; Darden, H.; Lee, H.; Pedersen, L. G. *J. Chem. Phys.* **1995**, 103, 8577.

- (38) Martínez, J. M.; Martínez, L. *J. Comput. Chem.* **2003**, *24*, 819.
- (39) Jorgensen, W. L.; Maxwell, D. S.; Tirado-Rives, J. *J. Am. Chem. Soc.* **1996**, *118*, 11225.
- (40) (a) Rizzo, R. C.; Jorgensen, W. L. *J. Am. Chem. Soc.* **1999**, *121*, 4827. (b) McDonald, N. A.; Jorgensen, W. L. *J. Phys. Chem. B* **1998**, *102*, 8049. (c) Kaminski, G.; Duffy, E. M.; Matsui, T.; Jorgensen, W. L. *J. Phys. Chem.* **1994**, *98*, 13077.
- (41) (a) Takagi, T. *Rev. Phys. Chem. Jpn.* **1978**, *48*, 10. (b) Muringer, M. J. P.; Trappeniers, N. J.; Biswas, S. N. *Phys. Chem. Liq.* **1985**, *14*, 273. (c) Takagi, T.; Teranishi, H. *Thermochim. Acta* **1989**, *141*, 291. (d) Takagi, T.; Sawada, K.; Urakawa, H.; Ueda, M.; Cibulka, I. *J. Chem. Eng. Data* **2004**, *49*, 1652.
- (42) Jacobson, B. *Acta Chem. Scand.* **1952**, *6*, 1485.
- (43) Reid, R. C.; Prausnitz, J. M.; Sherwood, T. K. *The Properties of gases and liquids*; McGraw-Hill: New York, 1977.
- (44) Joback, K. G.; Reid, R. C. *Chem. Eng. Commun.* **1987**, *57*, 233.
- (45) (a) Moens, L.; Blake, D. M.; Rudnicki, D. L.; Hale, M. J. *J. Sol. Energy Eng.* **2003**, *125*, 112. (b) Wu, B.; Reddy, R. G.; Rogers, R. D. *Proceedings of Solar Forum 2001*; Washington, DC, 2001. (c) Camacho, E. F.; Berenguel, M.; Rubio, F. R. *Advanced control of solar plants*; Springer-Verlag: London, 1997.
- (46) Hildebrand, J. H.; Prausnitz, J. M.; Scott, R. L. *Regular and related solutions*; Van Nostrand: New York, 1970.
- (47) Barton, A. F.; Knight, A. R. *J. Chem. Soc., Faraday Trans.* **1996**, *92*, 753.
- (48) Barton, A. F. *Handbook of Solubility Parameters*; CRC Press: Boca Raton, 1983.
- (49) Jackson, J. D. *Classical Electrodynamics*; Wiley: New York, 1999.
- (50) Ihmehls, E. C.; Gmehling, J. *Ind Eng. Chem. Res.* **2001**, *40*, 4470.
- (51) (a) Cibulka, I. *Fluid Phase Equilib.* **1993**, *89*, 1. (b) Fandiño, O.; Pensado, A. S.; Lugo, L.; López, E. R.; Fernández, J. *Green Chem.* **2005**, *7*, 775. (c) Gomes de Azevedo, R.; Esperanca, J. M. M. S.; Najdanovic-Visak, V.; Visak, Z. P.; Guedes, H. J. R.; Nunes da Ponte, M.; Rebelo, L. P. N. *J. Chem. Eng. Data* **2005**, *50*, 997. (d) Gu, Z.; Brennecke, J. F. *J. Chem. Eng. Data* **2002**, *47*, 339. (f) Morrow, T. I.; Maginn, E. J. *J. Phys. Chem. B* **2002**, *106*, 12807.
- (52) (a) Rebelo, L. P. N.; Najdanovic-Visak, V.; Visak, Z. P.; Nunes da Ponte, M.; Szydlowski, J.; Cerdeiría, C. A.; Troncoso, J.; Romaní, L.; Esperanca, J. M. S. S.; Guedes, H. J. R.; de Sousa, H. C. *Green Chem.* **2004**, *6*, 369. (b) Taravillo, M.; Baonza, V. G.; Cáceres, M.; Nuñez, J. *J. Phys.: Condens. Matter* **2003**, *15*, 2979.
- (53) Dack, M. R. *J. Chem. Soc. Rev.* **1975**, *4*, 211.
- (54) Stull, D. R. *Ind. Eng. Chem.* **1947**, *39*, 517.
- (55) Ambrose, D.; Walton, J. *Pure Appl. Chem.* **1989**, *61*, 1395.
- (56) Pamies, J. C.; Vega, L. F. *Mol. Phys.* **2002**, *100*, 2519.
- (57) Kiselev, S. B.; Ely, J. F. *Fluid Phase Equilib.* **2000**, *174*, 93.
- (58) Pfohl, O.; Budich, M. *Fluid Phase Equilib.* **2001**, *189*, 179.